J. Fluid Mech. (2008), *vol.* 596, *pp.* 21–47.
doi:10.1017/S0022112007009329 Printed in the United Kingdom

Dense flows of cohesive granular materials

PIERRE G. ROGNON[1,2], JEAN-NOËL ROUX[1], MOHAMED NAAÏM[2] AND FRANÇOIS CHEVOIR[1]

[1]LMSGC, Institut Navier, 2 allée Kepler, 77 420 Champs sur Marne, France
[2]CEMAGREF, 2 rue de la Papeterie, BP 76, 38402 Saint-Martin d'Hères, France
chevoir@lcpc.fr

(Received 27 April 2007 and in revised form 24 September 2007)

Using molecular dynamic simulations, we investigate the characteristics of dense flows of model cohesive grains. We describe their rheological behaviour and its origin at the scale of the grains and of their organization. Homogeneous plane shear flows give access to the constitutive law of cohesive grains which can be expressed by a simple friction law similar to the case of cohesionless grains, but intergranular cohesive forces strongly enhance the resistance to the shear. Then we show the consequence on flows down a slope: a plugged region develops at the free surface where the cohesion intensity is the strongest. Moreover, we measure various indicators of the microstructure within flows which evidence the aggregation of grains owing to cohesion and we analyse the properties of the contact network (force distributions and anisotropy). This provides new insights into the interplay between the local contact law, the microstructure and the macroscopic behavior of cohesive grains. Movies are available with the online version of the paper.

1. Introduction

Dense flows of cohesionless grains have a rich rheological behaviour, as has been pointed out during the last 20 years or so. However, real granular materials often present significant inter-particular cohesive forces resulting from different physical origins: *van der Waals forces* for small enough grains such as clay particles, powders (Rietema 1991; Quintanilla, Castellanos & Valverde 2003; Castellanos 2005) or third bodies in tribology (Iordanoff *et al* 2001, 2002), *capillary forces* in humid grains as in unsaturated soils or wet snow, and *solid bridges* in sintered powders (Miclea *et al.* 2005) or when liquid menisci freeze (Hatzes *et al.* 1991). How do these cohesive forces affect dense granular flows? Up to now, this question has been largely ignored.

In this paper, we provide new insights into the understanding of dense flows of cohesive grains. Flow characteristics are investigated through discrete numerical simulations (with a standard molecular dynamics method) which enable us to easily control the intensity of cohesion and provide information at the level of the grains, most often inaccessible to experiments. We simulate model cohesive grains with a simple intergranular adhesive force which captures the main feature of any cohesion model, the tensile strength of contacts. From homogeneous plane shear flows, prescribing pressure and shear rate, we measure a strong evolution of the constitutive law as the intergranular cohesion is increased, and we relate this macroscopic behaviour to the micro-mechanical properties of the grains and their microstructural organization. The understanding of the effect of intergranular cohesive force on constitutive law enables us to discuss practically relevant flows down inclined planes, which are more complex since stresses are no longer homogeneous.

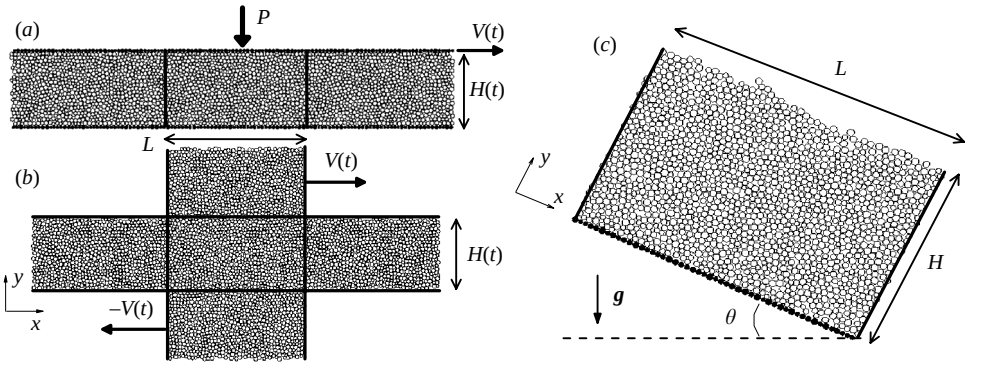

FIGURE 1. Flow geometries: plane shear (*a*) between two rough walls and (*b*) without wall; (*c*) rough inclined plane; (—) periodic boundary conditions, (black grains) rough walls.

Section 2 presents the knowledge about the effect of cohesion on granular flows. The flow geometries and the interaction model are described in § 3. From homogeneous plane shear flows and using dimensionless parameters identified in § 4, the macroscopic constitutive law of cohesive grains is measured and expressed in a simple manner in § 5. The consequences of this constitutive law for flows down rough inclined planes are discussed in § 6. We then come back to plane shear flows in § 7, to describe various microstructural quantities which evidence the development of space–time heterogeneities as the cohesion is increased (this can be observed on movies available with the online version of the paper). The link between the evolution of the microstructure and the macroscopic behaviour is given in § 8. Conclusions are drawn in § 9.

2. Background

Granular flows are currently a very active research domain motivated by fundamental issues (see for example Hutter & Rajagopal 1994; Rajchenbach 2000) as well as practical needs such as the transport of minerals, cereals or powders (Rietema 1991), or in geophysical applications: rock falls, landslides (Campbell, Cleary & Hopkins 1995), pyroclastic flows (Félix & Thomas 2004) and snow avalanches (Bouchet *et al.* 2003; Rognon *et al.* 2007) involve large-scale flows of particulate solids.

2.1. *Dense flow of cohesionless grains*

Up to now, most studies on granular flows have focused on cohesionless grains, and both experimental and numerical approaches have provided a good understanding of their behaviour in various geometries (see for example the review by GDR MiDi 2004). Among them, homogeneous plane shear and inclined plane highlighted some unusual flow characteristics (figure 1).

Using discrete simulations, da Cruz *et al.* (2005) investigated the behaviour of two dimensional quasi-rigid grains of mass m submitted to plane shear, prescribing pressure P and shear rate $\dot{\gamma}$. Depending on the single inertial number $I = \dot{\gamma}\sqrt{m/P}$, they highlighted three flow regimes called *quasi-static* when grain inertia is negligible ($I \lesssim 10^{-3}$), *collisional* when the medium is agitated and dilute ($I \gtrsim 0.3$), and, between these two extremes, *dense* when grain inertia is important with a contact network percolating through particles. They pointed out a simple expression for the constitutive law in this dense flow regime: the apparent friction coefficient $\mu^* = \tau/P$ linearly

increases with the inertial number I:

$$\mu^* = \mu^*_{min} + bI. \tag{2.1}$$

Both parameters μ^*_{min} and b depend on the properties of the grains. Also using discrete simulations of plane shear flow, Campbell (2002) distinguished two kinds of dense flow depending on the contact stiffness of the grains: an *elastic–inertial* regime for rather soft grains and an *inertial–non-collisional* regime for rather rigid grains.

Several experimental and numerical studies focused on the flows of cohesionless grains down inclined planes (see for example Pouliquen & Chevoir 2002; Pouliquen & Forterre 2002). Flows stop if the slope θ is lower than a critical slope ($\theta < \theta_{stop}$), accelerate if the slope is higher than θ_{acc} and, in between these two limits, reach a steady and uniform regime in which stress components vary along the flow depth y hydrostatically: $[P(y), \tau(y)] \propto (H - y)[\cos\theta, \sin\theta]$. According to the constitutive law (2.1) integrated in this stress field, the shear-rate profile follows a Bagnold scaling:

$$\dot{\gamma}(y) \propto (\theta - \theta_{stop})\sqrt{H - y}, \tag{2.2}$$

with some deviation toward a constant shear-rate profile for a thin flowing layer (Azanza 1998; Silbert *et al.* 2001; Prochnow 2002).

2.2. *Effect of cohesive force on macroscopic behaviour*

It is well known that cohesion strongly affects the mechanical properties of a granular material in the solid regime (see for example, Nedderman 1992). At the other extreme, the collisional regime of cohesive grains can be described well by extension of the kinetic theory (Kim & Arastoopour 2002). By contrast, how cohesion affects the dense flow behaviour previously described is much less well understood.

Static properties of a cohesive piling are extremely sensitive to its preparation, since depending on the quantity of agitation during the assembling phase, the cohesive sample is more or less heterogeneous. This loose structure is evidenced in plastic flows or in the compaction of the sample (see for example, Gilabert, Roux & Castellanos 2007). The macroscopic shear strength τ_{max} of the granular packing is strongly enhanced by cohesion (Richefeu, El Youssoufi & Radjaï 2006; Taboada, Estrada & Radjaï 2006). This is usually described by the Coulomb criterion, $\tau_{max} = \mu_c P + C$ where μ_c is the apparent friction coefficient of the assembly submitted to pressure P, and C represents the macroscopic intensity of cohesion, which Rumpf (1958) has related to the microstructure (solid fraction and coordination number) and the strength of inter-granular cohesive force. Cohesion also strongly increases the angle of avalanches, above which a static assembly of grains flows, and the angle of repose, below which the flow stops. This has been shown through rotating-drum experiments using wet glass beads (Fraysse, Thomé & Petit 1999; Tegzes *et al.* 1999; Nase *et al.* 2001; Bocquet, Charlaix & Restagno 2002) as well as powders (Castellanos *et al.* 1999, 2001; Valverde, Castellanos & Ramos 2000), through heap flow experiments (Mason *et al.* 1999; Samandani & Kudrolli 2001), and through crater experiments and simulations using wet glass beads or powder (Hornbaker *et al.* 1997; Tegzes *et al.* 1999; Nase *et al.* 2001; Mattutis & Schinner 2001).

Castellanos *et al.* (1999, 2001) showed that dense flows cannot be achieved using grains that are too small such as fine powders ($d \lesssim 10^{-4}$ m), since they are directly fluidized by the interstitial fluid from a solid to a suspension of fragile clusters. However, dense cohesive flows can be experimentally observed with large enough grains such as wet glass beads (as in Nase *et al.* 2001; Tegzes, Viczek & Schiffer 2002, 2003), or with natural snow (Rognon *et al.* 2007). Rotating-drum experiments using

	n	L/d	H/d
Plane shear with walls	2000	50	40–60
Plane shear without walls	800	40	20–30
Inclined plane	1500	50	$\sim$30

TABLE 1. Size of simulated systems: length L, height H and number of grains n.

wet glass beads or powders highlighted the development of correlated motion which leads to an irregular free surface and an increase of avalanche size (Samandani & Kudrolli 2001; Tegzes *et al.* 2002, 2003; Alexander *et al.* 2006). Discrete simulations also pointed out the aggregation of cohesive grains in various flow geometries (Ennis, Tardos & Pfeffer 1991; Talu, Tardos & Ruud van Ommen 2001; Weber, Hoffman & Hrenya 2004), which was evidenced by measuring the increasing fluctuation of local solid fraction (Mei *et al.* 2000) or the increasing time of contact between grains (Brewster *et al.* 2005). Using annular shear flows, Klausner (2000) measured an increase of the apparent friction coefficient of powders from 0.2 for rather weak cohesion, up to 0.8 for rather strong cohesion. This cohesion enhanced friction was also observed in plane shear simulations by Iordanoff, Fillot & Berthier (2005), Aarons & Sundaresan (2006) and Alexander *et al.* (2006). Brewster *et al.* (2005) simulated the flow of a thick layer of cohesive grains down an inclined plane, and pointed out a breakdown of the Bagnold scaling for the shear-rate profile (2.2) owing to the development of a plugged region at the surface of the flow, whose thickness increases with cohesion.

Existing studies thus indicate that cohesion stongly affects the behaviour of dense granular flow as well as its microstructure. However, the constitutive law of dense cohesive flow has not yet been formulated, and the interplay between microstructure and macroscopic behaviour is still an open question.

3. Simulated system

The review by GDR MiDi (2004) revealed a good agreement between two-dimensional simulations and three-dimensional experiments of cohesionless granular flows. Consequently, we choose to simulate two-dimensional systems which favour low computational time without affecting the results qualitatively. The granular material is an assembly of n disks of average diameter d and average mass m. A small polydispersity ($\pm 20\,\%$) is introduced to prevent crystallization.

3.1. *Flow geometry*

Two flow geometries are studied: the homogeneous plane shear (without gravity) and the rough inclined plane. The length L and the height H of the simulated systems are summarized in table 1. In both cases, periodic boundary conditions are applied along the flow direction (x) and rough walls are made of contiguous grains sharing the characteristics of the flowing grains: the same polydispersity and mechanical properties (especially the same cohesion), but without rotation.

Plane shear flows are performed prescribing pressure and shear rate through two kinds of boundary conditions along the transverse direction y. First, the material is sheared between two parallel rough walls at a distance of H apart (figure 1*a*). One wall is fixed while the other moves at the prescribed velocity V. The other method was introduced by Lees & Edwards (1972) to avoid wall perturbations: it consists

in applying periodic boundary conditions along y, as shown in figure 1(b). The top and bottom cells move with a velocity $\pm V(t)$, which is adapted at each time step t to maintain a constant shear rate $\dot{\gamma} = V(t)/H(t)$. The control of the pressure is achieved by allowing the dilatancy of the shear cell along y (H is not fixed), either through the motion of the moving wall, or through a global dilation of the cell (in the absence of walls). The evolution of H is: $\dot{H} = (P_0 - P)L/g_p$ (Campbell 2005; Gilabert *et al.* 2007), where g_p is a viscous damping parameter, and P_0 is the pressure exerted by the grains on the moving wall, or the average pressure in the shear cell (in the absence of walls). Steady state corresponds to $\langle P_0 \rangle = P$, where $\langle\rangle$ denotes an average over time.

Flows down a rough inclined plane are driven by gravity $\boldsymbol{g}$ (figure 1c). Grains constitute a layer of thickness H flowing along a rough inclined wall (slope θ).

3.2. *Contact law*

Let us consider the contact between two grains i and j of diameter $d_{i,j}$, mass $m_{i,j}$, centred at position $\boldsymbol{r}_{i,j}$, with velocity $\boldsymbol{v}_{i,j}$ and rotation rate $\omega_{i,j}$. We call the reduced mass $m_{ij} = m_i m_j/(m_i + m_j)$ and the reduced diameter $d_{ij} = d_i d_j/(d_i + d_j)$). Let $\boldsymbol{n}_{ij}$ denote the normal unit vector, pointing from i to j ($\boldsymbol{n}_{ij} = \boldsymbol{r}_{ij}/||\boldsymbol{r}_{ij}||$ with the notation $\boldsymbol{r}_{ij} = \boldsymbol{r}_j - \boldsymbol{r}_i$), and $\boldsymbol{t}_{ij}$ a unit tangential vector such that $(\boldsymbol{n}_{ij}, \boldsymbol{t}_{ij})$ is positively oriented.

The intergranular force $\boldsymbol{F}_{ij}$ exerted by the grain i onto its neighbour j is split into its normal and tangential components, $\boldsymbol{F}_{ij} = N_{ij}\boldsymbol{n}_{ij} + T_{ij}\boldsymbol{t}_{ij}$. The *contact law* relates N_{ij} and T_{ij} to the corresponding components of relative displacements and/or velocities. The relative velocity at the contact point is equal to $\boldsymbol{V}_{ij} = \boldsymbol{v}_i - \boldsymbol{v}_j + 1/2(d_i\omega_i + d_j\omega_j)\boldsymbol{t}_{ij}$. Its normal component $V_{ij}^N = \boldsymbol{n}_{ij} \cdot \boldsymbol{V}_{ij}$ is the time derivative of the normal deflection of the contact (or apparent overlap of undeformed disks): $h_{ij} = (d_i + d_j)/2 - ||\boldsymbol{r}_{ij}||$. Its tangential component $V_{ij}^T = \boldsymbol{t}_{ij} \cdot \boldsymbol{V}_{ij}$ is the time derivative of the tangential relative displacement δ_{ij}. The normal contact force is the sum of three contributions, an elastic one N^e, a viscous one N^v, and a cohesive one N^a.

The linear (unilateral) elastic law is $N_{ij}^e = k_n h_{ij}$ with a normal elastic stiffness coefficient k_n related to the Young's modulus E of the grains: $k_n \sim Ed$ (Hertz 1881). A normal viscous force is added to dissipate energy during collisions: $N_{ij}^v = \zeta_{ij}\dot{h}_{ij}$ with a damping coefficient ζ_{ij} related to the restitution coefficient e in a binary collision of cohesionless grains: $\zeta_{ij} = \sqrt{m_{ij}k_n}(-2\ln e)/\sqrt{\pi^2 + \ln^2 e}$.

The different models which represent the various physical origins of cohesive interaction generally oppose the repulsive force with an attractive force $N^a(h)$. The shape of the total static normal force $N(h) = N^e(h) + N^a(h)$ involves at least three parameters: a maximum attractive force N^c, an equilibrium deflection h^c (for which $N(h^c) = 0$), and a range D of the attractive interaction ($N^a(h) = 0$ for $h \leqslant -D$). Direct adhesion between solid surfaces associated to van der Waals forces was characterized well in Tabor (1981), Kendall (1993, 1994) and Gady, Schleef & Reifenberger (1996). It can be fully described by the model of Maugis (1992) whose two limits give rise to the simpler models plotted in figure 2(a). The *DMT* (Derjaguin, Muller & Toporov 1975) and the *JKR* (Johnson, Kendall & Roberts 1971) models, respectively, apply for soft or hard grains whose contacts are slightly or strongly deformed by cohesion. In the *DMT* model, the attractive force $N^a(h)$ is constant and its range D is null. In the *JKR* model, the attractive force is proportional to the contact area, and a neck forms when the grains recede for $-D \leqslant h \leqslant 0$, thereby leading to a hysteresis. The capillary cohesion was fully described experimentally in Pitois (1999) and Bocquet *et al.* (2002), and theoretically in Elena *et al.* (1999) and Chateau, Moucheront & Pitois (2002). It also presents a hysteresis which corresponds to the difference between the formation and the breaking distance of a liquid meniscus (figure 2b). In both

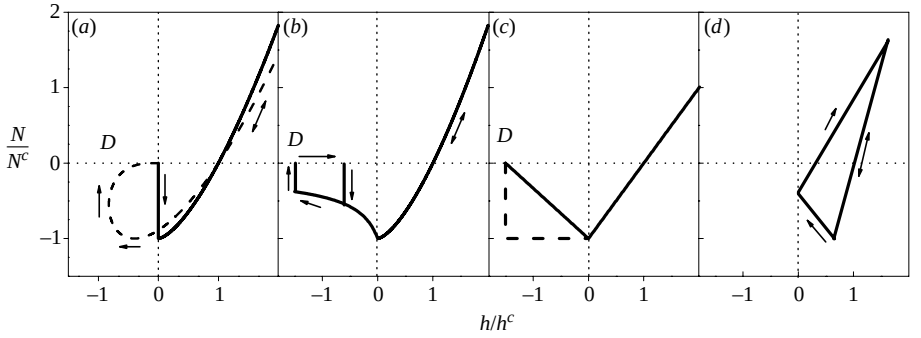

FIGURE 2. Common cohesive interactions: (*a*) DMT (—) and JKR (- - -) models, (*b*) capillary force; simplified models used in numerical simulation: (*c*) linear (—) and square (- - -), (*d*) plasticity.

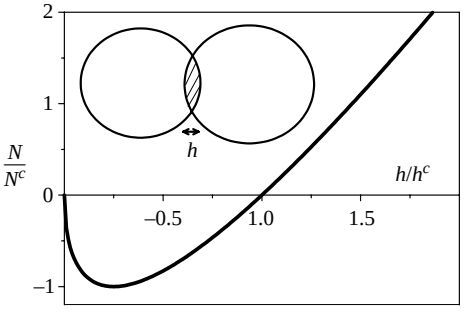

FIGURE 3. Cohesion model used in the present paper: normal force N/N^c versus normal deformation h/h^c (inset: apparent interpenetration).

cases, the roughness of the surface plays an important role in cohesive contact. The asperities decrease the effective surface where the short-range van der Waals force is significant (see Fuller & Tabor 1975; Thornton 1997; Tomas 2004), and, in the case of humid grains they give rise to different scales of liquid menisci (Bocquet *et al.* 2002). Moreover their plastic deformation leads to the ageing process for the contact (Ovarlez & Clément 2003). In their simulations, Gilabert *et al.* (2007), Kadau *et al.* (2002) and Weber *et al.* (2004) approximated these models of cohesion by the simple functions plotted in figure 2(*c*), and Luding, Tykhoniuk & Thomas (2003) and Richefeu *et al.* (2005) used a more complex function which takes into account the contact plasticity (figure 2*d*).

We choose a simple cohesive force which captures the main feature of the previous cohesion models: the maximum attractive force N^c. We consider the limit of $D=0$ and we do not take into account any hysteretic behaviour or contact plasticity. As previously proposed by Mattutis & Schinner (2001) and Radjaï, Preechawuttipong & Peyroux (2001), we choose the smooth function:

$$N_{ij}^a(h_{ij}) = -\sqrt{4k_n N^c h_{ij}}. \tag{3.1}$$

In the static limit ($N_{ij}^v = 0$), this model leads to a maximum attractive force N^c and to an equilibrium deflection $h^c = 4N^c/k_n$ (see figure 3). Richefeu *et al.* (2005) showed that the shape of $N^a(h)$ does not have an influence provided it leads to the same N^c.

Polydispersity	μ	e	k_t/k_n
$\pm 20\%$	0.4	0.1	0.5

TABLE 2. Fixed material parameters.

In Rognon *et al.* (2006), we compared the previous function $N^a(h)$ with the DMT model $N^a(h) = -N^c$ and checked that they give rise to similar flow properties.

As usual (Radjaï *et al.* 2001; Richefeu *et al.* 2005; Wolf *et al.* 2005; Gilabert *et al.* 2007), friction between grains is described by a Coulomb condition enforced with the sole elastic part of the normal force:

$$|T_{ij}| \leqslant \mu N^e_{ij}, \tag{3.2}$$

where μ is the coefficient of friction between grains. The tangential component of the contact force is related to the elastic part δ^e_{ij} of the relative tangential displacement δ_{ij}: $T_{ij} = k_t \delta^e_{ij}$, with a tangential stiffness coefficient k_t. δ^e_{ij} satisfies:

$$\dot{\delta}^e_{ij} = \begin{cases} 0 & \text{if } |T_{ij}| = \mu N^e_{ij} \text{ and } T_{ij} V^T_{ij} > 0, \quad (3.3a) \\ V^T_{ij} & \text{otherwise}, \quad (3.3b) \end{cases}$$

and vanishes when the contact opens. The contact is termed *sliding* in (3.3*a*) (the condition that T_{ij} and V^T_{ij} share the same sign ensuring a positive dissipation due to friction) and *sticking* in (3.3*b*). Rolling friction could also be considered (Gilabert *et al.* 2007). However, this mechanism is significant for very small particles, $< 1\,\mu$m (Jones *et al.* 2004). For much larger particles ($\sim 100\,\mu$m), this mechanism should not be relevant. In fact, an analysis of the influence of rolling friction, keeping sliding friction, was performed in Gilabert *et al.* (2007) in the case of the isotropic compaction of an assembly of cohesive grains, and it was found that the inclusion of small rolling friction has only a small effect.

Table 2 summarizes the material parameters which are fixed in all our calculations. The friction coefficient between grains is fairly realistic ($\mu = 0.4$), except in § 8.2 where the case of frictionless grains ($\mu = 0$) is discussed. $e = 0.1$ corresponds to a rather strongly dissipative material, which favours dense flows. da Cruz *et al.* (2005) showed that the values of μ and e do not significantly affect the characteristics of cohesionless granular flows, except for the extreme case $\mu = 0$. Johnson (1985) showed that k_t is of the same order of magnitude as k_n, and Silbert *et al.* (2001) and Campbell (2002) pointed out that it has a very small influence on the results for cohesionless grains. k_t is then fixed to $k_n/2$ in all our calculations. The values of the stiffness coefficient k_n and of the maximum attractive force N^c will be discussed in § 4.

3.3. *Simulation method*

Numerical simulations are carried out with the molecular dynamics method, as in Cundall & Strack (1979), Silbert *et al.* (2001), Roux & Chevoir (2005) and da Cruz *et al.* (2005). The equations of motion are discretized using a standard procedure (Gear's order-three predictor–corrector algorithm, Allen & Tildesley 1987). The time step is chosen equal to $\tau_c/50$ where τ_c is the collision time for a pair of cohesionless equal-sized grains: $\tau_c = \sqrt{m(\pi^2 + \ln^2 e)/(4k_n)}$.

4. Dimensional analysis

The grains and the flow geometries are described by a list of independent parameters. It is convenient to use dimensional analysis to extract dimensionless numbers which express the relative importance of different physical phenomena and enable quantitative comparison with real materials.

Grains are described by their diameter d, mass m, coefficient of restitution e and coefficient of friction μ, elastic stiffness parameters k_n and k_t and maximum attractive force N^c. The terms d and m, respectively, constitute the length and mass scales. Since the dimensionless number μ, e and k_t/k_n are fixed, there remain two dimensional parameters that describe grains: k_n and N^c. The flow geometries are described either by the gravity $\boldsymbol{g}$, the slope θ and the thickness H of the flowing layer for the inclined plane, or by the prescribed pressure P, the prescribed shear rate $\dot{\gamma}$, and the viscous damping parameter g_p for plane shear. The dimensionless number $g_p/\sqrt{mk_n}=1$ is chosen, which ensures that the time scale of the fluctuations of H is imposed by the material rather than the wall, and the wall sticks to the material. Consequently, the shear state is described by pressure P and shear rate $\dot{\gamma}$. Among the various possible choices (see Campbell 2002; da Cruz *et al.* 2005), we use the following dimensionless numbers.

4.1. *Inertial number I*

Da Cruz *et al.* (2005) and GDR MiDi (2004) showed that the shear state of cohesionless rigid grains is controlled by the single inertial number I, combination of the shear rate $\dot{\gamma}$ and of the pressure P, whose expression is (for a two-dimensional system):

$$I=\dot{\gamma}\sqrt{\frac{m}{P}}. \tag{4.1}$$

I compares the inertial time $\sqrt{m/P}$ with the shear time $1/\dot{\gamma}$ and is called *inertial number*. Small values ($I \lesssim 10^{-3}$) correspond to the *quasi-static* regime where the grain inertia is not relevant. Inversely, large values ($I \gtrsim 0.3$) correspond to the *collisional* regime where grains interact through binary collisions.

4.2. *Cohesion numbers Bo_g and η*

Different dimensionless numbers are used to quantify the intensity of cohesion. They compare the maximum attractive force N^c to a typical force scale in the system. In the presence of gravity, Nase *et al.* (2001) introduced the *granular Bond number*:

$$Bo_g=\frac{N^c}{mg}, \tag{4.2}$$

which compares N^c with the weight of a grain. For plane shear flows without gravity, we define (as in Wolf *et al.* 2005; Gilabert *et al.* 2007) another dimensionless number η:

$$\eta=\frac{N^c}{Pd}, \tag{4.3}$$

which compares N^c with the average normal force Pd due to the pressure. According to this definition, the transition between a regime of low cohesion and a regime of high cohesion should depend on η and should occur for η of order unity. Let us now estimate of the parameter η in realistic three-dimensional situations, $\eta=N^c/(Pd^2)$. N^c can be estimated by $\pi\gamma_l d$ in the case of humid grains (where γ_l is the surface tension of the liquid, of the order of $0.05\,\mathrm{N\,m^{-1}}$) and by $Ad/(24z_0^2)$ in the case of van der Waals adhesion (where A is the Hamaker constant, of the order of $10^{-19}\,\mathrm{N\,m}$ and

Plane shear			Inclined plane			
I	η	h_0^*	H/d	θ	Bo_g	h_0^*
$10^{-2} \to 0.3$	$0 \to 85$	10^{-5}	≈ 30	$14^\circ \to 39^\circ$	$0 \to 200$	10^{-6}

TABLE 3. Ranges of dimensionless numbers explored.

z_0 a molecular distance, of the order of 2 Å). In the presence of gravity, the pressure P is given by $\rho_p \nu g H$, at the bottom of a layer of height $H = Nd$, with a solid fraction $\nu \approx 0.6$. Considering glass beads for which $\rho \approx 2500\,\mathrm{kg\,m^{-3}}$, we obtain $\eta \approx 10^{-5}/(Nd^2)$ for capillary cohesion and $\eta \approx 7\ 10^{-8}/(Nd^2)$ for van der Waals adhesion (where d is expressed in m). This means that a value of $\eta \approx 100$ at the bottom of a layer of 10 grains is relevant if $d = 10^{-4}$ m for capillary cohesion or if $d = 10^{-5}$ m for van der Waals adhesion. However, this estimation does not take into account the screening of cohesion by the roughness of the grains.

4.3. *Stiffness number h^**

The third dimensionless number measures the average relative deformation of the contacts in the system: $h^* = h/d$. Without cohesion, this deformation is merely due to the pressure and limited by the stiffness: $h_0^* = P/k_n$. Cohesive force enhances this deformation:

$$h^*(\eta) = h_0^* \mathscr{H}(\eta), \tag{4.4}$$

with $\mathscr{H}(\eta) = 1 + 2\eta + 2\sqrt{\eta + \eta^2}$. For strong cohesion, h^* measures the deformation of grains due to the sole cohesive force (without pressure): $N^c/(k_n d)$ and ranges from 10^{-5} for powders (Israelachvili 1992; Aarons & Sundaresan 2006) down to $\approx 10^{-12}$ for wet glass beads.

4.4. *Range of dimensionless numbers explored*

Plane shear flows are performed prescribing six values of I between 10^{-2} and 0.3 and 36 values of η from cohesionless grains, $\eta = 0$, up to $\eta = 85$ (table 3). It was shown that the properties of cohesionless granular packings as well as flow characteristics do not depend on the value of h_0^* once it is small enough ($h_0^* \lesssim 10^{-4}$) (Roux & Combe 2002; da Cruz *et al.* 2005). We choose $h_0^* = 10^{-5}$ so that the systems are in this *rigid limit* at least for low cohesion: $h^*(\eta) \leqslant 10^{-4}$ for $\eta \leqslant 2.5$. For larger values of η, there might be an influence of the deformation of the grains, which is specifically discussed in Campbell (2002) and Aarons & Sundaresan (2006). However, lowering the value of h_0^* below 10^{-5} would strongly increase computational time.

Flows down inclines are performed with slopes varying between 15° and 39°, and with a thickness $H = 30d$, in order to obtain steady and uniform regimes. Six value of Bo_g are set starting from cohesionless grains, $Bo_g = 0$, up to $Bo_g = 200$. This corresponds to the range of Bo_g which was experimentally reached by Nase *et al.* (2001) varying the size of glass beads ($0.5 < d < 10\,\mathrm{mm}$, $\rho \approx 2500\,\mathrm{kg\,m^{-3}}$) and the surface tension of the liquid ($40 < \gamma_l < 72\,\mathrm{mN\,m^{-1}}$).

5. Measurement of the macroscopic constitutive law

Using homogeneous plane shear flows, we present in this section the measurement of the effect of cohesive force on the macroscopic behaviour of grains. Such a method was successfully used to measure the rheological behaviour of cohesionless grains (see

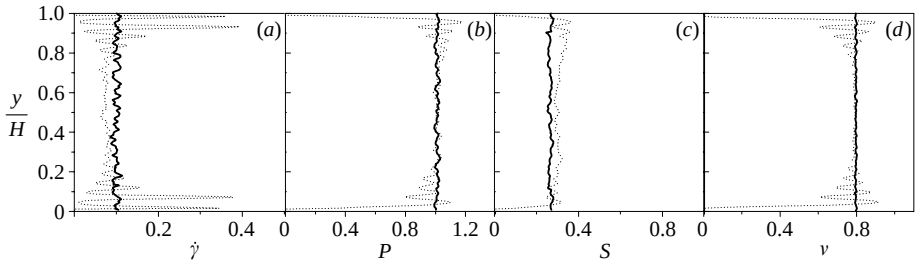

FIGURE 4. Homogeneous shear state ($P = 1$, $\dot{\gamma} = 0.1$, $N^c = 0$): (a) shear rate $\dot{\gamma}(y)$, (b) pressure $P(y)$, (c) shear stress $S(y)$ and (d) solid fraction $\nu(y)$; transverse boundary conditions with walls (...) and without wall (—).

for example Campbell 2002; da Cruz *et al.* 2005), and to explore the effect of grain stiffness on cohesive flows (Aarons & Sundaresan 2006).

5.1. *Steady homogeneous shear state*

The preparation which has been used most of the time consists in starting from a configuration where the disks are randomly deposited without contact and without velocity. The average solid fraction is around 0.5. Then the prescribed shear rate and the prescribed pressure are applied. After a sufficient amount of time, the flowing layer reaches a steady shear state characterized by constant time-averaged kinetic energy, stress tensor and solid fraction. This contrasts with the static case (Gilabert *et al.* 2007), where if P is slowly decreased, a hysteresis is observed, with a microstructure which strongly depends on the maximum value of P applied to the packing in the past. These steady flows do not depend on the initial solid fraction or on the initial velocity profile (plug or linear). A great advantage of the bi-periodic boundary conditions is that the convergence toward a steady state is around ten times faster than with walls.

When a continuous steady state is reached, the simulation is carried out during a sufficient amount of time Δt, so that the relative displacement of two neighbouring layers is larger than around ten grains ($\dot{\gamma}\Delta t \geqslant 10$). In this steady state, we consider that the statistical distribution of the quantities of interest (structure, velocities, forces...) are independent of time and uniform along the flow direction, so that we proceed to an average in space along the flow direction and in time by 100 time steps distributed over the period Δt. Using averaging methods described in Lätzel, Luding & Hermann (2000) and Prochnow (2002), figure 4 plots the profiles of solid fraction $\nu(y)$, shear rate $\dot{\gamma}(y)$, pressure $P(y)$ and shear stress $S(y)$. The stress tensor is dominated by the term associated with contact forces between grains (da Cruz *et al.* 2005):

$$\underline{\underline{\Sigma}} = \frac{1}{LH}\mathrm{Sym}\left(\sum_{i<j} \boldsymbol{F}_{ij} \otimes \boldsymbol{r}_{ij}\right). \tag{5.1}$$

For every steady and homogeneous shear flows, we observe that $\Sigma_{xx} \simeq \Sigma_{yy}$, implying that stress tensors share common principal directions. Consequently, the pressure P given by $(\Sigma_{xx} + \Sigma_{yy})/2 \approx \Sigma_{yy}$.

Figure 4 also compare the profiles for the two kinds of boundary condition, with and without walls. Except in the five first layers near the walls, where the granular material is organized, the two kinds of boundary condition give rise to consistent shear states. Even when starting from a localized velocity profile near one of the walls, we systematically observed a relaxation toward a homogeneous shear state.

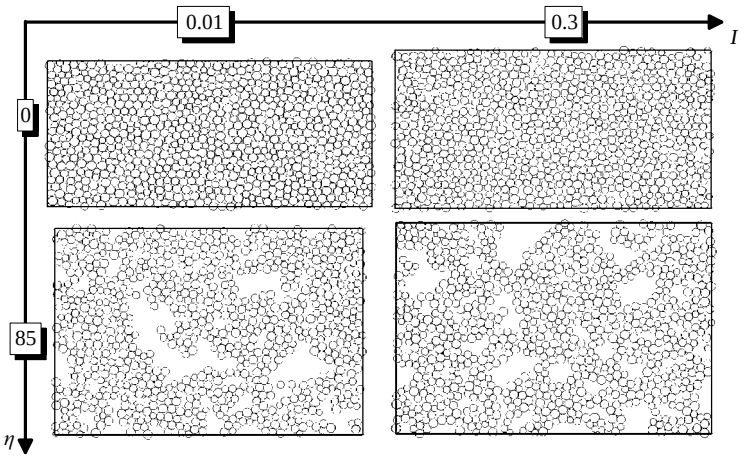

FIGURE 5. Homogeneous plane shear flows: picture from simulations for different values of inertial number I and cohesion intensity η. Movies of the flows are available with the online version of the paper.

The conclusion is that the granular material is completely sheared and that the shear is homogeneous. This allows us to define average (along time and space) solid fraction ν, shear rate $\dot{\gamma}$, pressure P and shear stress S. The following measurements are made in the whole system using simulations without walls.

In the range of I and η explored (see table 3), the flows are homogeneous as was previously described. Figure 5 shows some such flows. For strong enough cohesion (η larger than around 100), the shear state becomes heterogeneous. Between two walls, the flow is made up of a single rigid block which sticks alternately to one of the two walls (Forsyth, Hutton & Rhodes 2002; Iordanoff *et al.* 2005). In the absence of walls, the shear is localized in a few layers between two rigid assemblies. These localized shear flows would require specific studies. They are not discussed in this paper.

5.2. *Constitutive law*

The homogeneous shear states give direct access to the rheological law of the granular materials through the measurement of two fundamental dimensionless quantities, the solid fraction ν and the apparent friction coefficient $\mu^* = S/P$, which adjust in response to the two prescribed dimensionless numbers: the inertial number ($0.01 \leqslant I \leqslant 0.3$) and the cohesion number ($0 \leqslant \eta \leqslant 85$). For cohesionless grains, the influence of I on ν and μ^* was measured by da Cruz *et al.* (2005). We will show the strong influence of the cohesion number η on those two quantities.

Friction law is the variations of the effective friction coefficient μ^* as a function of I and η (figure 6*a*). The first general observation is that cohesion strongly increases μ^*, up to large values ($\mu^* \approx 2$). Da Cruz *et al.* (2005) showed that the apparent friction coefficient of cohesionless granular materials increases approximately linearly with I, starting from a minimum value μ^*_{min}: $\mu(I) \simeq \mu^*_{min} + bI$, with a possible saturation for large I. We observe that this law may be extended to cohesive grains:

$$\mu^*(I, \eta) \simeq \mu^*_{min}(\eta) + b(\eta)I. \tag{5.2}$$

Figure 6(*b*) plots both functions $\mu^*_{min}(\eta)$ and $b(\eta)$, which have the same shape. Below a cohesion threshold ($\eta \lesssim 10$) the cohesion does not affect μ^*_{min} or b. Above this threshold, $\mu^*_{min}(\eta)$ and $b(\eta)$ strongly increase.

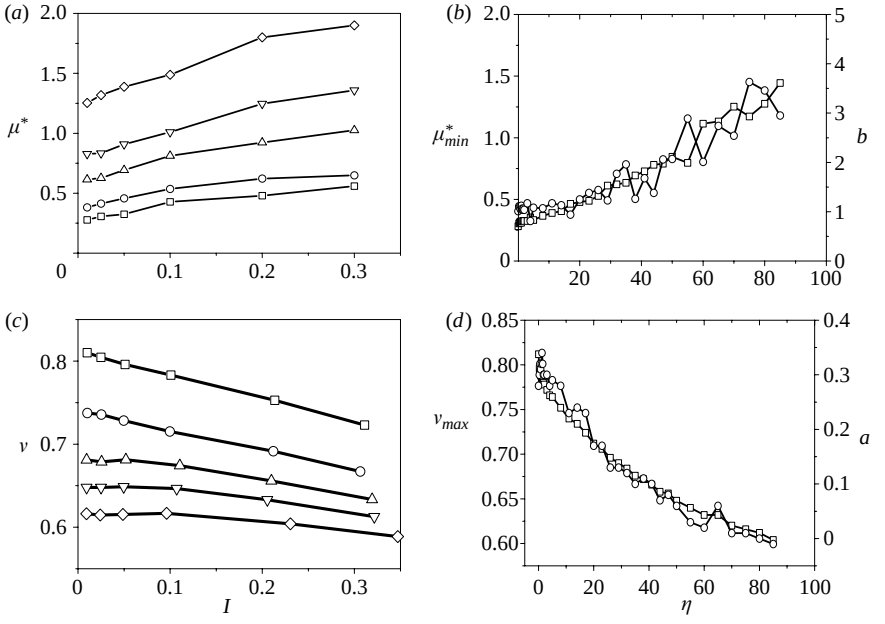

FIGURE 6. Friction and dilatancy laws. (a, c) $\mu^*(I)$ and $\nu(I)$ for $\eta = 0$ (□), 10 (○), 30 (△), 50 (▽), 70 (◇); (b) $\mu^*_{min}(\eta)$ (□) and $b(\eta)$ (○); (d) $\nu_{max}(\eta)$ (□) and $a(\eta)$ (○).

Dilatancy law is the variations of the solid fraction ν as a function of I and η (figure 6*c*). The first general observation is the strong expansion of the material owing to cohesion. Da Cruz *et al.* (2005) showed that the solid fraction of cohesionless granular materials decreases approximately linearly as a function of I, starting from a maximum value ν_{max}: $\nu(I) \simeq \nu_{max} - aI$. We observe that this law may be extended to cohesive grains:

$$\nu(I, \eta) \simeq \nu_{max}(\eta) - a(\eta)I. \tag{5.3}$$

Figure 6(*d*) plots both functions $\nu_{max}(\eta)$ and $a(\eta)$ which have the same shape. They strongly decrease for weak cohesion $\eta \lesssim 2$, then still decrease, but more slowly. On the one hand, the decrease of $\nu_{max}(\eta)$ means that cohesion tends to dilate the flows, especially for low η. On the other hand, the decrease of $a(\eta)$, down to zero for the highest cohesion, means that the solid fraction no longer depends on the inertial number I for strong cohesion.

Starting from both variations of solid fraction and apparent friction as functions of I and η, we show (figure 7) the variation of the apparent friction as a function of solid fraction instead of I and η. We observe an approximate collapse of the data on a master curve made of complementary zones of high solid fraction (low η) and smaller solid fraction (higher η). The apparent friction strongly decreases when the solid fraction increases. This tendency of the data, which was previously observed for cohesionless grains by Craig, Buckholz & Domoto (1986) and da Cruz *et al.* (2005), appears as a robust feature which shows the importance of the solid fraction in granular flows and may be of help in rheological models (see for example Josserand, Lagree & Lhuillier 2004).

The constitutive law is usually written as the dependencies of the pressure and shear stress on the shear rate and solid fraction. With cohesion, we should also include the dependency on the cohesion intensity η. From the definition of I (4.1) and the

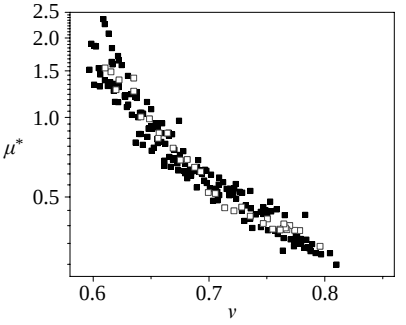

FIGURE 7. Variation of the apparent friction coefficient μ^* as a function of solid fraction ν measured in plane shear flows for various η and I. □, data for a constant inertial number $I = 0.05$ and various η.

friction law (5.2), this leads to the following expression of the shear stress S:

$$S = \mu^*_{min}(\eta)P + b(\eta)\sqrt{mP}\dot{\gamma}, \tag{5.4}$$

which corresponds to a viscoplastic constitutive law, with a Coulomb friction term and a viscous term. The apparent viscosity $b(\eta)\sqrt{mP}$ depends on the cohesion intensity through the parameter $b(\eta)$ (figure 6*b*). We shall then define a *low cohesion regime* ($\eta \lesssim 10$) where the cohesion does not affect the apparent viscosity and a *high cohesion regime* ($\eta \gtrsim 10$) where the apparent viscosity is strongly enhanced by cohesion.

5.3. *Quasi-static limit*

In the quasi-static limit ($I \to 0$), the extrapolation of the constitutive law (5.4) predicts that $S = \mu^*_{min}(\eta)P$. Figure 6(*b*) shows that $\mu^*_{min}(\eta)$ is roughly linear, $\mu^*_{min} + \alpha\eta$ with $\alpha \approx 0.012$, so that constitutive law can be expressed as:

$$S = \mu^*_{min}P + \alpha N^c/d. \tag{5.5}$$

This is reminiscent of the Coulomb criterion described in § 2.2. μ^*_{min} then identifies to the apparent friction coefficient μ_c and $\alpha N^c/d$ to the macroscopic intensity of cohesion C. Assuming that all the contacts break at the shear threshold, Rumpf (1958) related C to the microstructure (solid fraction ν and coordination number Z) and the strength of inter-granular cohesive force N^c through the following formula (written in two dimensions): $C = Z\nu N^c\mu_c/\pi d$. Considering the following values ($Z \approx 3$, $\nu \approx 0.8$, $\mu_c \approx \mu^*_{min} \approx 0.3$) provides $C \approx 0.2N^c/d$. The form is similar, but the factor α estimated from quasi-static flows is much smaller (by a factor around 20) than the value predicted by the Rumpf formula. We shall try to interpret this difference in § 8.4, after having analysed the microstructure of the flow.

6. Cohesive flows down an inclined plane

It is clear that the homogeneous plane shear cannot be achieved in real situations because of gravity g. Nevertheless, it provided a good understanding of the macroscopic behaviour which can now be used to discuss flows down inclined planes. This geometry is closer to practical needs, but more complex since stresses are no longer homogeneous along the depth. This section presents the behaviour of cohesive grains flowing down a rough inclined plane, focusing on a steady and uniform regime. The dimensionless number that measures the cohesion intensity is the granular Bond number Bo_g, defined in § 4.

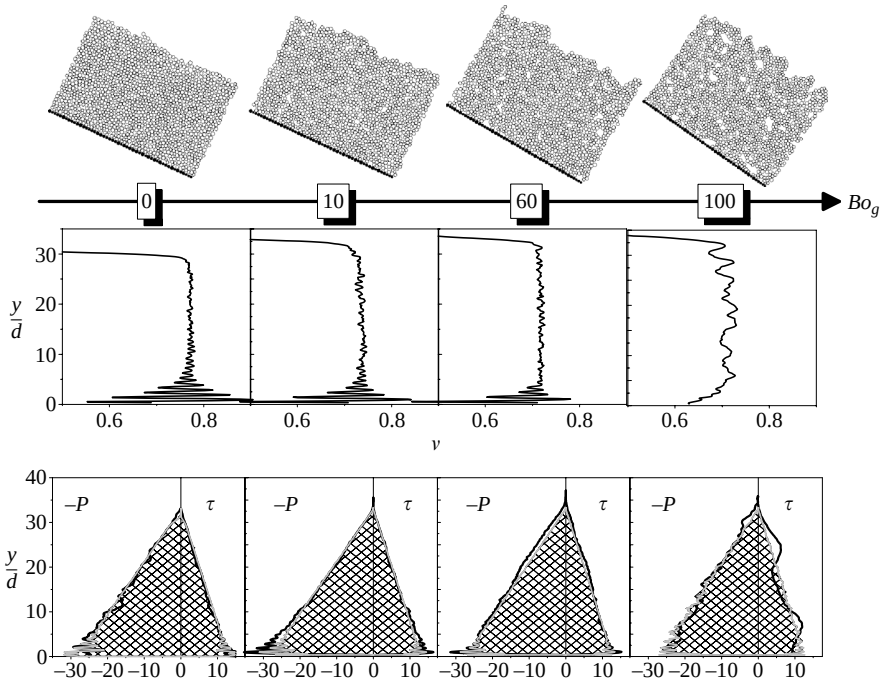

FIGURE 8. Steady and uniform flows down inclined plane ($\theta = 25°$, $H/d \approx 30$). For different values of the granular Bond number Bo_g, profiles of solid fraction $\nu(y)$ and comparison of profiles of measured stresses P and τ (—) with hydrostatic stresses P^h and $-\tau^h$ (surface). For clarity, pressures are plotted along the negative values and shear stresses along the positive values.

6.1. *Steady and uniform flow regimes*

An important feature of cohesionless granular flows down inclines is that they reach a steady and uniform regime in a large range of slope (Pouliquen 1999). In this regime, friction exactly compensates the gravity driving force. In presence of cohesion, this regime also exists, as detailed in this section.

The preparation which was used most of the time consists in starting from an initial configuration where the disks are randomly deposited without contact and without velocity. The average solid fraction is around 0.5. Then gravity is applied so that the plane is inclined with a slope θ. After a sufficient time, the flowing layer may reach a steady shear state characterized by constant time-averaged kinetic energy, stress tensor and solid fraction. A second method consists in starting from a steady uniform regime at given slope and cohesion, then changing either slope or cohesion. The final flow does not depend on the initial state.

Figures 8 plots the profiles of solid fraction, stresses and velocity along the depth for flows of similar thickness ($H \approx 30d$), same slope ($\theta = 25°$), but with different cohesion Bo_g. Without cohesion ($Bo_g = 0$), as previously shown by Silbert *et al.* (2001) and Prochnow (2002), the solid fraction $\nu(y)$ is constant along the depth except for a thin layer (a few grains) near the rough wall where oscillations reveal the organization of grains in layers. As cohesion increases, $\nu(y)$ remains constant in the bulk and oscillates near the wall, but its mean value decreases. Figure 8(*b*) compares the stresses measured within the flow using (5.1) with the hydrostatic stresses under gravity: $[P^h(y), \tau^h(y)] = \rho_p g \int_{y_1=0}^{y} \nu(y_1)\, \mathrm{d}y_1 [\cos\theta, -\sin\theta]$ and reveals a

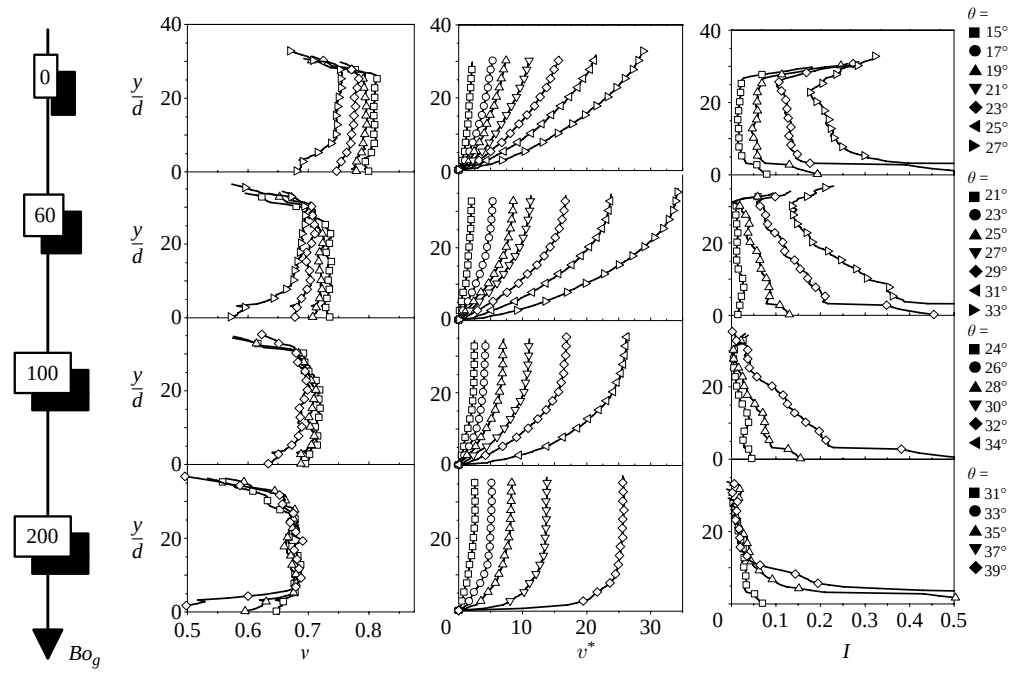

FIGURE 9. For various slopes and various cohesion intensities, profiles of solid fraction, velocity v^* (in units of $\sqrt{gd}$) and inertial number I.

good agreement (ρ_p is the mass density of the grains). Shear stress τ compensates the gravity stress τ^h, which reveal that the flow is in a uniform regime. Neglecting the small fluctuations of the solid fraction around its mean value ν, stresses follow:

$$\begin{pmatrix} P(y) \\ \tau(y) \end{pmatrix} = \rho_p g \nu (H - y) \begin{pmatrix} \cos\theta \\ \sin\theta \end{pmatrix}. \tag{6.1}$$

Consequently, the apparent friction coefficient $\mu^* = \tau(y)/P(y)$ is constant along the depth and directly prescribed by the slope: $\mu^* = \tan\theta$. Furthermore, since the pressure increases along the depth, the cohesion number η varies according to $\eta(y) = Bo_g d/(\nu \cos\theta (H - y))$ so that the cohesion increases close to the free surface.

6.2. *Constitutive law deduced from flows down inclines*

Steady and uniform flows down inclines consist in applying through the slope θ an apparent friction coefficient $\mu^* = \tan\theta$ to the material. The local constitutive law of the granular material can be deduced from the measurements of the inertial number profiles at various slope. The following method is used to explore different slopes: for various cohesive intensity Bo_g, steady and uniform flows are initially performed at a given slope; then, the slope is decreased (or increased) at a low enough rate so that flows can be considered as steady and uniform at each time step, until the flows stop (or accelerate). Figure 9 plots the profiles of solid fraction, velocity and inertial number I for various slopes and cohesion intensities Bo_g. According to the relation $\mu^*(\nu)$ (§ 5.2), the solid fraction is set by the slope and is constant along the depth (except near the free surface and near the rough base). Without cohesion, as shown by Silbert *et al.* (2001), the velocity profile satisfies the Bagnold scaling, since the inertial number is approximately constant along the depth, except in the first few bottom layers where I increases (probably because of the organization of the grains in layers

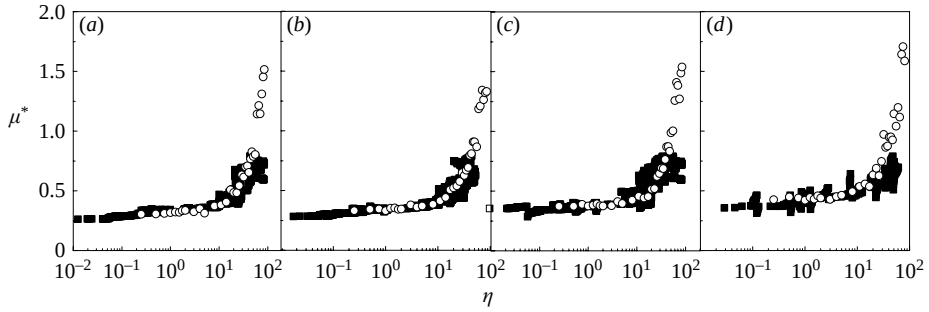

FIGURE 10. Constitutive law measured in plane shear flows (○) and in flows down an inclined plane (■); $\mu^*(\eta)$ for $I =$ (*a*) 0.01, (*b*) 0.025, (*c*) 0.05, (*d*) 0.1.

near the wall, leading to a sliding velocity), and the first few free-surface layers where I diverges owing to the low pressure. With cohesive force, the shear rate drops to zero in a solid layer near the free surface. The thickness of this layer increases as Bo_g increases. This breakdown of the Bagnold scaling, observed by Brewster *et al.* (2005), is evidenced by the variation of the inertial number which is no longer constant along the depth, and drops to zero in the solid surface layer. Since each layer into the flows is submitted to a shear with a prescribed $\mu^* = \tan\theta$, but a varying cohesion intensity $\eta(y)$, the constitutive law can be deduced by measuring the inertial number profile $I(y)$ and extracting $\mu^*(I(y), \eta(y))$. Figure 10 plots $\mu^*(\eta)$ for various I, and compares the results obtained using an inclined plane with the constitutive law measured using plane shear flows. Results are in good agreement, although data from the inclined plane are scattered. This is not surprising since they are not averaged over time, nor over the transverse direction. The great difference between these two approaches is that the shear rate is prescribed in plane shear whereas the shear stress is prescribed in flows down an inclined plane. As a consequence, large value of I combined with strong cohesion, which can be explored using plane shear, cannot be reached within flow down an inclined plane since the most cohesive part of the flow is plugged. Since the apparent viscosity of cohesive grains is strongly enhanced by cohesion above $\eta \gtrsim 10$, but is not affected for lower values, the thickness of the plugged layer is of the order of $Bo_g/10$ grains.

7. Microstructure

The two previous sections have shown the strong effect of cohesion on the macroscopic rheological law. We now turn to the evolution of the microstructure of the flow. As shown in figure 5, when the intensity of cohesion increases, large voids appear, separating dense areas. This was also observed in Mei *et al.* (2000) and Weber *et al.* (2004). Experimentally, Tegzes *et al.* (2002, 2003) observed correlated motions of grains in dense flows of humid grains. There is a large amount of published work on the formation of aggregates in agitated dilute systems, such as fluidized powders (Castellanos *et al.* 2001) or coagulation of dusts in astrophysical situation (Dominik & Tielens 1997). In the present section, we measure various microstructural indicators showing the development of space–time heterogeneities within the granular flow submitted to homogeneous plane shear.

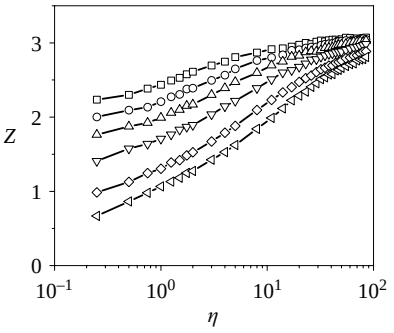

FIGURE 11. Coordination number Z. $I = 0.01$ (□), 0.025 (○), 0.05 (△), 0.1 (▽), 0.2 (◇), 0.3 (◁).

7.1. *Coordination number Z*

The first quantitative indicator is the average number of contacts per grain, the coordination number Z. The variations of Z as a function of I and η are shown in figure 11. In the low-cohesion regime ($\eta \lesssim 10$), Z increases strongly when I decreases and tends to a maximum value when $I \to 0$. This is consistent with the dilatancy of the granular material when going from the quasi-static regime to the collisional regime. This behaviour is similar to that observed with cohesionless grains (da Cruz *et al.* 2005). For higher cohesion, the dependency of Z on I becomes smaller, and Z is around 2.5 even for the highest value of I. This indicates that cohesion tends to increase the value of I for the transition between dense and collisional regimes.

As cohesion increases, the coordination number first strongly increases while $\eta \lesssim 5$, then increases more slowly to reach a maximum value. The increase of $Z(\eta)$ whereas the solid fraction $\nu(\eta)$ decreases is unexpected, and reveals that cohesive grains agglomerate in dense areas where the coordination number is high, while, on the whole, the granular material is becoming more porous, which decreases the average solid fraction.

7.2. *Distribution of local solid fraction, length scale ℓ^{ν}*

As a way to characterize quantitatively the increasing heterogeneity of density induced by cohesion, we measured the distribution of the local solid fraction (Richard *et al.* 2003; da Cruz *et al.* 2005). At each time step, we performed a radical tessellation. The local solid fraction around each grain is defined as the ratio of the areas of the grain and of its Voronoi cell (the points which are closer from this grain than from any other grain). This defines the field of the local solid fraction $\nu(\boldsymbol{r})$. Figure 12(a) shows the distribution of the local solid fraction for a given I and for various η. The small polydispersity allows high values of solid fraction ($\nu(\boldsymbol{r}) \to 0.9$). With cohesion, dense areas still exist, whereas the local solid fraction of the grains close to the voids decreases ($\nu(\boldsymbol{r}) \to 0.2$). The standard deviation $\Delta\nu$ of the distribution may be used to characterize the heterogeneity of density. Figure 12(b) shows that cohesion enhances $\Delta\nu$.

The auto-correlation $F(\boldsymbol{R})$ of the fluctuating solid fraction field $\delta\nu(\boldsymbol{r})$:

$$F(\boldsymbol{R}) = \frac{\langle \delta\nu(\boldsymbol{r})\delta\nu(\boldsymbol{r}+\boldsymbol{R})\rangle}{\delta\nu^2}, \tag{7.1}$$

gives access to a characteristic length scale of the heterogeneities, associating dense areas and voids. We observe that F is isotropic, and apart from a small peak around $R = d$, decreases approximately exponentially with R (figure 12c). In order to quantify

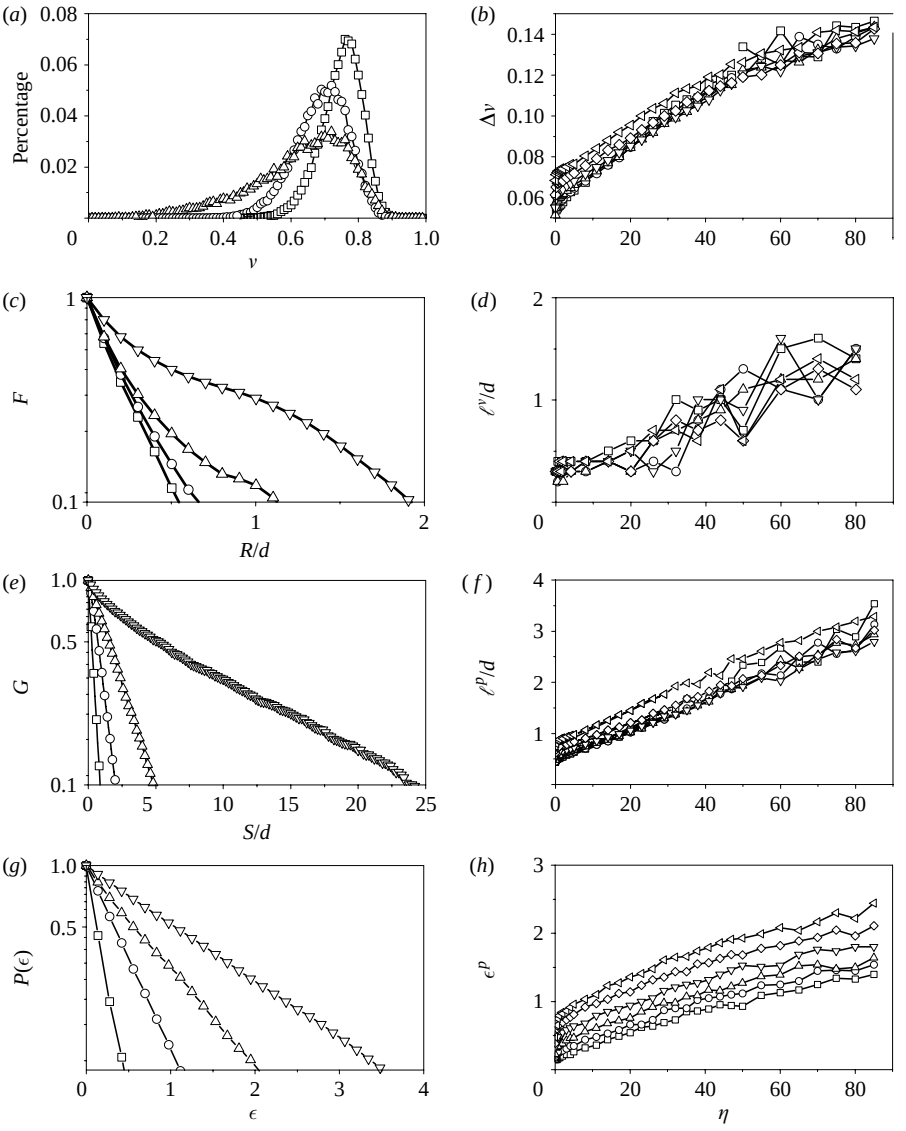

FIGURE 12. Heterogeneity of the microstructure. (a, b) Distribution of local solid fraction and its standard deviation $\Delta\nu(\eta)$. (c, d) Correlation of the local solid fraction $F(R)$ and associated length scale ℓ^{ν}/d. (e, f) Distribution of pore size $G(S)$ and associated length scale ℓ^{p}/d. (g, h) Persistence of contacts $P(\epsilon)$ and typical strain of persistence $\epsilon^{p}(\eta)$. (a, c, e, g) $I = 0.2$, $\eta = 0$ (□), 10 (○), 30 (△), 80 (▽). (b, d, f, h) $I = 0.01$ (□), 0.025 (○), 0.05 (△), 0.1 (▽), 0.2 (◇), 0.3 (◁).

this effect, we define the correlation length ℓ^{ν} as the distance where the correlation is equal to 0.4 (other values give similar qualitative results). Figure 12(d) shows that cohesion enhances ℓ^{ν}.

7.3. *Distribution of porosity, length scale* ℓ^{p}

Another indicator of the organization of the granular material is given by the distribution of pore sizes. The first step is a discretization of the picture of the granular flow at each time step, with a pixel size of $d/20$. This allows us to distinguish the pixels lying on voids from those lying on grains. Then, using an invasion algorithm,

it is possible to make a list of the connected voids, and to measure their area S. Figure 12(e) shows the proportion of void space $G(S)$ belonging to a pore of area larger than S. $G(S)$ decreases approximately exponentially with S: $G(S) \simeq \exp(-S/S^p)$. Then $\ell^p = \sqrt{S^p}$ characterizes the length scale of the pores, but does not account for their anisotropy (the pores may be elongated). Figure 12(f) shows that cohesion strongly enhances ℓ^p. This length also increases with the inertial number, which is not surprising because increasing I decreases the solid fraction (dilatancy law), i.e increases the void fraction, and so the connecting void probability.

7.4. *Persistence of contacts, strain scale* ϵ^p

ℓ^v and ℓ^p provide information on the spatial organization of the granular material. We now present another quantity associated to the time correlation of the contact network. Starting from a population of contacts at time t, we define the function $P(T)$ as the proportion of contacts which have not been broken at the time $t+T$ (an average over time t is performed). We notice that a similar quantity, called topological correlation function was defined in Choi *et al.* (2004), to measure the diffusion in granular flows. This function obviously starts from the value 1. Figure 12(g) shows that it decreases exponentially to zero with time T or the associated strain $\epsilon = \dot{\gamma} T$: $P(\epsilon) \approx \exp(-\epsilon/\epsilon^p)$. ϵ^p is the characteristic strain scale of persistent contacts. Figure 12(h) shows that ϵ^p is lower than 1 for cohesionless grains, and that cohesion increases it above 1. This means that the persistent time of the contacts becomes larger than the shear time.

7.5. *Velocity correlations, length scale* ℓ^v

Correlated motions of grains and transient rigid clusters were evidenced with cohesionless grains (Bonamy *et al.* 2002; GDR MiDi 2004; Pouliquen 2004), and found to affect the rheological properties of the granular flows (Ertas & Halsey 2002; Mills, Rognon & Chevoir 2005). Pouliquen (2004) measured the fluctuating velocity field $\delta \boldsymbol{v}(\boldsymbol{r})$ at the surface of a flow down an inclined plane and showed that its correlation length ℓ^v strongly increases as the inclination decreases near jamming. This observation suggests that the jamming mechanism is connected to the development of space–time correlations within the flow when going from the collisional regime to the quasi-static regime. It is then tempting to measure this correlation length ℓ^v within a homogeneous shear flow, as a function of the two dimensionless numbers I and η.

We start by measuring the auto-correlation function $C(\boldsymbol{R})$ of the fluctuating velocity field $\delta \boldsymbol{v}(\boldsymbol{r})$:

$$C(\boldsymbol{R}) = \frac{\sum_{i,j} \delta v_i \delta v_j g(\boldsymbol{r}_{ij} - \boldsymbol{R})}{\sum_{i,j} g(\boldsymbol{r}_{ij} - \boldsymbol{R})}, \tag{7.2}$$

where $\delta v_i = |\delta \boldsymbol{v}_i|$, and g is a Gaussian function of width $w = 0.4d$. We checked that the results do not depend significantly on w, and are qualitatively the same when considering only one component of $\delta \boldsymbol{v}$. We observe that $C(\boldsymbol{R})$ is isotropic and decreases exponentially with R: $C(R) \propto \exp(-R/\ell^v)$, which defines the correlation length ℓ^v.

Figure 13(a) shows ℓ^v as a function of I for cohesionless grains. Consistently with the measurements down an inclined plane performed by Pouliquen (2004), ℓ^v strongly increases when the inertial number I decreases, that is to say when going from the dense regime to the quasi-static regime. Figure 13(b) shows ℓ^v as a function of η for three values of I. For $I \gtrsim 0.1$, ℓ^v is small for cohesionless grains and increases as a function of η. Conversely, for small I, there are already correlated motions for

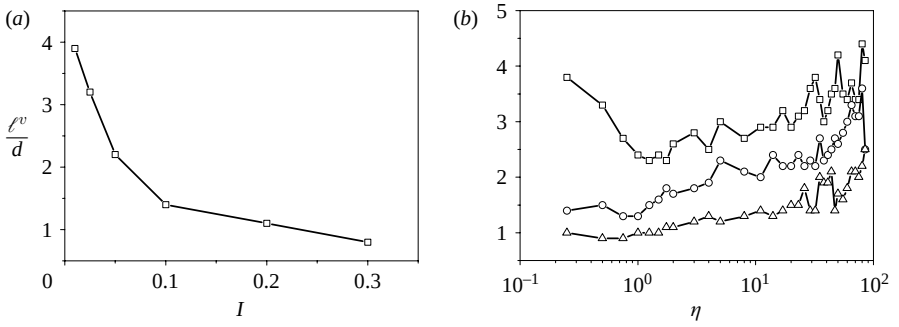

FIGURE 13. Correlation of velocity fluctuations : (*a*) $\ell^v(I)$, $\eta = 0$, (*b*) $\ell^v(\eta)$, $I = 0.01$ (□), 0.1 (○), 0.3 (△).

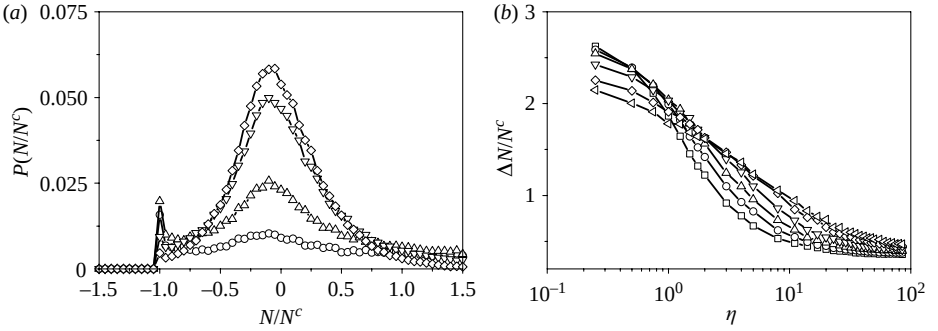

FIGURE 14. (*a*) Distribution of normal force: $\eta = 1$ (○), 10 (△), 30 (▽), 85 (◇). (*b*) Dispersion $\Delta N/N^c(\eta)$: $I = 0.01$ (□), 0.025 (○), 0.05 (△), 0.1 (▽), 0.2 (◇), 0.3 (◁).

cohesionless grains, then as η increases, there is first an expansion of the material which decreases ℓ^v before an increase for larger η.

8. Links between the microstructure and the macroscopic behaviour

In § 5, we have shown the strong effect of the cohesion number η on two macroscopic quantities, the apparent friction μ^* and the solid fraction ν. Then, in § 7, we have measured the dependencies of several indicators of the microstructure of the granular flow ($Z, \ell^v, \ell^p, \ell^v, \epsilon^p$) as a function of η. Their increase is a clear signature of the development of space–time heterogeneities induced by cohesion. In this section, we focus on the relation between the evolution of the microstructure and of the macroscopic behaviour.

8.1. *Distribution of normal forces*

The cohesion seems to increase the apparent viscosity for η larger than around 10 (see § 5.2). This is surprising since estimating by Pd the normal traction force necessary to separate two cohesive grains would predict a high cohesion regime for $\eta \simeq 1$. However, this assumption is rather crude since, as in cohesionless granular pilings (Radjaï *et al.* 1996) or granular flows (O'Hern *et al.* 2001), we observe a large distribution of normal forces $N = N^e + N^a$. Figure 14(*a*) plots the distribution of N/N^c. In cohesive granular systems, N/N^c may be negative but is always larger than -1. For $\eta \leqslant 1$, the force scale Pd is larger than N^c: the distribution is broad, so that contacts may be broken easily. For much larger η, the force scale is given by N^c: the distribution

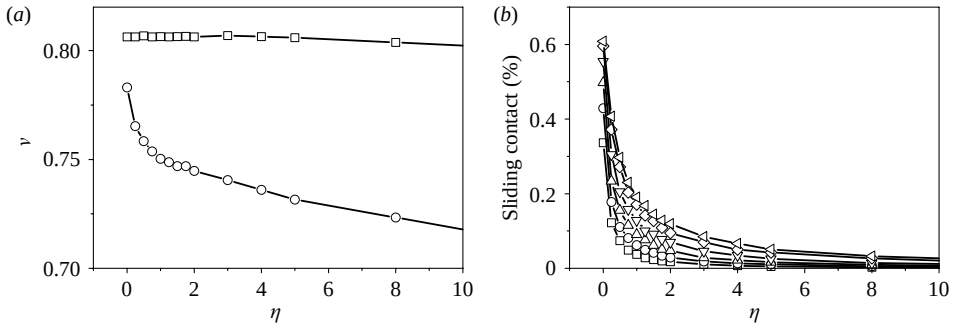

FIGURE 15. Increase of apparent friction: (*a*) solid fraction $\nu(\eta)$, $I = 0.2$, $\mu = 0.4$ (○), $\mu = 0$ (□); (*b*) proportion of sliding contacts: $I = 0.01$ (□), 0.025 (○), 0.05 (△), 0.1 (▽), 0.2 (◇), 0.3 (◁).

is much more peaked, so that most contacts cannot be broken. Figure 14(*b*) shows that the standard deviation of the distribution decreases slightly when I increases but decreases significantly when η increases. It becomes smaller than unity for η between 3 and 10. This suggests that the high cohesion regime transition might be controlled by the distribution of normal forces rather than by their average value.

8.2. *Increase of apparent friction*

Friction between grains is described by a Coulomb condition enforced with the sole elastic part of the normal force: $|T/N^e| \leqslant \mu$ (see § 3.2). When compared with the total normal force $N = N^e + N^a$, it is easy to show that $|T/N| \leqslant \mu\mathscr{H}(|N^c/N|)$, where the function $\mathscr{H}$ was defined in § 4.3. For $N \gg N^c$, which happens for small cohesion, $\mathscr{H} \simeq 1$. Then the apparent friction coefficient between grains remains μ. However, for $N \ll N^c$ which is frequent for large cohesion, $\mathscr{H} \simeq 4|N^c/N|$ which means that the apparent friction coefficient between grains is strongly increased. For cohesionless grains, it was shown that an increase of μ significantly decreases ν_{max} (da Cruz *et al.* 2005). Consequently, we predict that this increase of the apparent friction between grains induced by cohesion should result in an expansion of the granular flow. In order to evidence this effect, we have compared the evolution of the solid fraction for frictional ($\mu = 0.4$) and frictionless grains ($\mu = 0$) in figure 15(*a*). Contrarily to frictionless grains, the expansion of frictional grains starts for small η ($\eta \lesssim 2$). Consistently, this increase of apparent friction between grains strongly reduces the proportion of sliding contacts in the same range of η, as shown in figure 15(*b*). This suggests that conversion of sliding into sticking contacts might be responsible for this dilation (Rivier 2005).

8.3. *Anisotropy*

We now return to the friction law and analyse the strong increase of the apparent friction $\mu^*(\eta)$ above the agglomeration transition. It has been shown by Campbell & Brennen (1985) and da Cruz *et al.* (2005) that μ^* may be written as the sum of two contributions, associated to the angular distribution of normal and tangential forces:

$$\mu^* = -\int_0^\pi \zeta_N(\phi)\sin(2\phi)\,\mathrm{d}\phi + \int_0^\pi \zeta_T(\phi)\cos(2\phi)\,\mathrm{d}\phi. \tag{8.1}$$

ϕ is the direction of a contact counted counterclockwise from the flow direction, between 0 and π. ζ_N and ζ_T are the products of the distribution of contact orientations by the intensities of normal and tangential forces, respectively, normalized by the

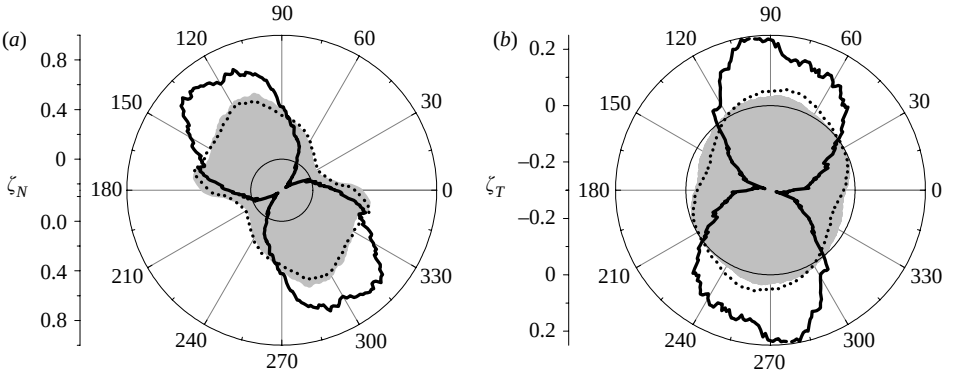

FIGURE 16. Polar histogram (negative value inside the small circle) of (a) normal forces $\zeta_N(\phi)$ and (b) tangential forces $\zeta_T(\phi)$: $I = 0.1$, $\mu = 0.4$, $\eta = 0$ (grey), $\eta = 1$ (..). $\eta = 50$ (–).

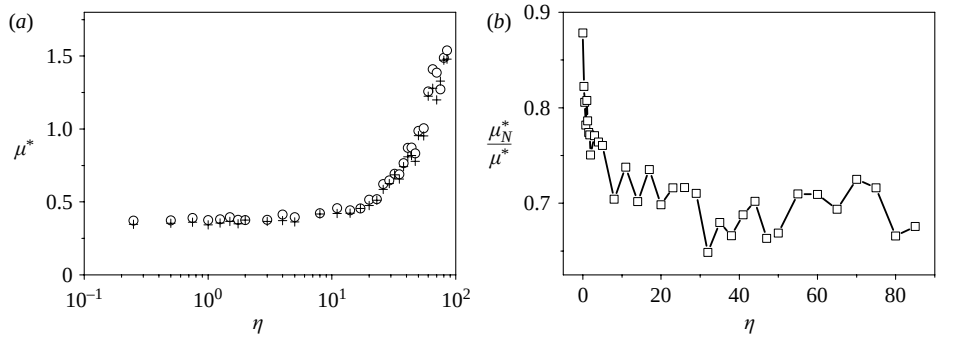

FIGURE 17. Apparent friction and anisotropy (a) Comparison between direct measurement (○) and calculation from (8.1). (+) ($I = 0.01$) (b) Relative contribution of normal force to the apparent friction.

average normal force in the system (figure 16). As expected, figure 17(a) shows that the calculation of the apparent friction using (8.1) is in excellent agreement with the direct calculation. Figure 17(a) highlights that both normal and tangential anisotropies significantly increase as a function of η, as was previously shown in quasi-static evolutions by Radjaï *et al.* (2001). The increase of the amplitude of ζ_N occurs for $\eta \gtrsim 10$, so that it seems related to the agglomeration transition: $\zeta_N(\phi)$ increases in the direction of force chain compression ($\phi \simeq 120$), but decreases and may even become negative in the direction of force chain traction ($\phi \simeq 30$). This evolution, strongly enhanced by the factor $\sin 2\phi$, leads to an increase of the normal contribution to the apparent friction μ_N^*. On the other hand, the enhancement of the amplitude $\zeta_T(\phi)$ starts for small η, so that it seems connected to the increase of apparent friction induced by cohesion. Also, this evolution, strongly enhanced by the factor $\cos 2\phi$, leads to an increase of the tangential contribution to the apparent friction μ_T^*. Figure 17(b) shows that the relative contribution of normal forces to the apparent friction μ_N^*/μ^* decreases with cohesion (going from around 90% for $\eta = 0$ to around 70% for $\eta \gtrsim 10$).

8.4. *Basic mechanisms*

We now summarize as simply as possible the previous quantitative analysis. The shear of dense cohesionless grains requires that each individual grain moves over

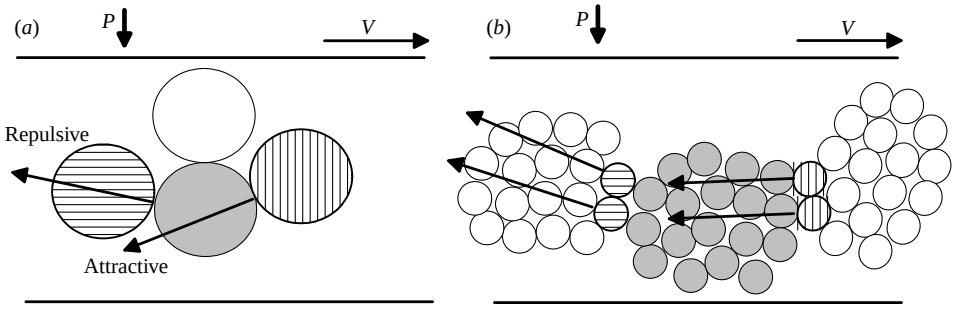

FIGURE 18. Basic mechanisms involved in cohesive granular flows: (*a*) without aggregates and (*b*) taking into account the agglomeration of grains.

the neighbouring grain in front of it (figure 18*a*). The macroscopic resistance to the shear is then merely due to the repulsive forces acting throughout the ascension. With cohesion, a second contribution enhances the macroscopic resistance to the shear: after the ascension, the cohesive contact must be broken. Naively, this reasoning predicts that the part of the shear stress due to cohesion should increase as the maximum attractive force is increased, and consequently that the part of the friction coefficient due to cohesion should increase as η increases. Our measurements show that when the cohesion intensity η increases from 0 to 85, μ^* increases from 0.25 to 3. However, the agglomeration of cohesive grains must also be taken into account. Then the previous mechanism where a grain moves over the neighbouring grain in front of it must be considered at the scale of the large clusters, rather than at the scale of individual grains (figure 18*b*). This leads to a strong expansion of the granular media since two scales of porosity appears: between and inside the clusters. Moreover, after the ascending phase, the separation of two clusters merely requires the contacts of the grains to be broken at the interface of the clusters, while the contacts inside the clusters are not broken. Consequently, the organization in clusters strongly favours the flow of cohesive grains.

The interpretation of the difference between our interpolation of the friction law in the quasi-static regime and the Coulomb criterion using the Rumpf formula is now clear: since the flowing granular materials is made of aggregates with enduring contacts, the contacts do not all break simultaneously when the material is flowing, but only those which are at the periphery of the aggregates. This may reduce the number of breaking contacts significantly. At the other limit, the aggregation of grains owing to cohesion may affect the transition between dense and collisional flow regimes. Cohesion favours multiple enduring contacts within aggregates, and whether there exists a regime with binary collision at high I is an open question which requires a specific study.

9. Conclusion

The existence of intergranular cohesive forces is found to affect dense granular flows strongly. The simulations of simple systems with a generic cohesion model enable us to identify the rheological behaviour of cohesive grains, and to provide a complete scheme on its origin at the scale of the grains and of their organization.

The simulation of a simple flow geometry, the homogeneous plane shear, and the use of dimensional analysis appear to be efficient in describing the behaviour of cohesive granular flows. We point out that their constitutive law can be expressed by

a simple friction law, similar to the case of cohesionless grains, but that the cohesion strongly enhances the resistance to the shear. The consequence on cohesive granular flow down a slope is that a plugged region develops at the free surface where the cohesion intensity is the strongest. Then, flows are made of a fluid bottom layer and a solid-like top layer, the thickness of which increases with the intergranular cohesive force.

Moreover, we reveal the strong interplay between the local contact law (friction and cohesion), the properties of the contact network (force distributions and anisotropy) and the rheological law (dilatancy and apparent friction). For small cohesion, owing to the increase of the apparent friction between grains, the proportion of sliding contacts decreases which induces expansion of the material. For larger cohesion, the agglomeration of the grains results in the growth of heterogeneities (large voids separating dense granular areas), and in the increase of the contact force anisotropy, which strongly enhances the resistance to the shear. Then, for larger cohesion, the granular material breaks apart.

This study is a first step toward the understanding of the rheology of cohesive granular materials. It is clear that further studies are necessary to take into account other specificities of cohesive forces (range of interaction, hysteresis, viscous dissipation in liquid bridges, solid bridges...). It would be extremely interesting to compare those predictions with physical experiments on model materials such as wet glass beads, or controlled powders in vacuum.

We gratefully acknowledge Ivan Iordanoff, Philippe Coussot, Anaël Lemaitre, Guillaume Ovarlez, Dietrich Wolf and Frédéric da Cruz for interesting discussions at various stages of this study. We thank Pierre-Olivier Camus for help in the numerical simulations. Laboratoire des Matériaux et Structures du Génie Civil is a joint laboratory, depending on Laboratoire Central des Ponts et Chaussées, Ecole Nationale des Ponts et Chaussées and Centre National de la Recherche Scientifique.

REFERENCES

Aarons, L. & Sundaresan, S. 2006 Shear flow of assemblies of cohesive and non-cohesive granular materials. *Powder Technol.* **169**, 10–20.

Alexander, A.W., Chaudhuri, B., Faqih, A., Muzzio, F. J., Davies, C. & Tomassone, M. S. 2006 Avalanching flow of cohesive powders. *Powder Technol.* **164**, 13–21.

Allen, M. P. & Tildesley, D. J. 1987 *Computer Simulation of Liquids*. Oxford University Press.

Azanza, E. 1998 Ecoulements granulaires bidimensionnels sur plan incliné. PhD thesis, Ecole Nationale des Ponts et Chaussées, Paris.

Bocquet, L., Charlaix, E. & Restagno, F. 2002 Physics of humid granular media. *C. R. Phys.* **3**, 207–215.

Bonamy, D., Daviaud, F., Laurent, L., Bonetti, M. & Bouchaud, J.-P. 2002 Multiscale clustering in granular surface flows. *Phys. Rev. Lett.* **89**, 034301.

Bouchet, A., Naaim, M., Ousset, F., Bellot, H. & Cauvard, D. 2003 Experimental determination of constitutive equations for dense and dry avalanches: presentation of the set-up and first results. *Surv. Geophys.* **24**, 525–541.

Brewster, R., Grest, G. S., Landry, J. W. & Levine, A. J. 2005 Plug flow and the breakdown of Bagnold scaling in cohesive granular flows. *Phys. Rev.* E **72**, 061301.

Campbell, C. S. 2002 Granular shear flows at the elastic limit. *J. Fluid Mech.* **465**, 261–291.

Campbell, C. S. 2005 Stress-controlled elastic granular shear flow. *J. Fluid Mech.* **539**, 273–297.

Campbell, C. S. & Brennen, C. E. 1985 Computer simulation of granular shear flows. *J. Fluid Mech.* **151**, 167–188.

Campbell, C. S., Cleary, P. W. & Hopkins, M. 1995 Large-scale landslide simulations: global deformation, velocity and basal friction. *J. Geophys. Res.* **100**, 8267–8284.

Castellanos, A. 2005 The relationship between attractive interparticule forces and bulk behavior in dry and uncharged fine powders. *Adv. Phys.* **54**, 263–376.

Castellanos, A., Valverde, J. M., Perez, A. T., Ramos, A. & Watson, P. K. 1999 Flow regimes in fine cohesive powders. *Phys. Rev. Lett.* **82**, 1156–1159.

Castellanos, A., Valverde, J. M. & Quintanilla, M. A. S. 2001 Aggregation and sedimentation in gas-fluidized beds of cohesive powders. *Phys. Rev.* E **64**, 041304.

Chateau, X., Moucheront, P. & Pitois, O. 2002 Micromechanics of unsaturated granular media. *J. Engng Mech.* **128**, 856–863.

Choi, J. C., Kudrolli, A., Rosales, R. R. & Bazant, M. Z. 2004 Diffusion and mixing in gravity-driven dense granular flows. *Phys. Rev. Lett.* **92**, 174301.

Craig, K., Buckholz, R. H. & Domoto, G. 1986 An experimental study of the rapid flow of dry cohesionless metal powders. *J. Appl. Mech.* **53**, 935.

da Cruz, F., Emam, S., Prochnow, M., Roux, J.-N. & Chevoir, F. 2005 Rheophysics of dense granular materials: discrete simulation of plane shear flows. *Phys. Rev.* E **72**, 021309.

Cundall, P. A. & Strack, O. D. L. 1979 A discrete numerical model for granular assemblies. *Géotech.* **29**, 47–65.

Derjaguin, B. V., Muller, V. M. & Toporov, Y. P. 1975 Effect of contact deformation on the adhesion of particules. *J. Colloid Interface Sci.* **53**, 314–326.

Dominik, C. & Tielens, A. G. G. M 1997 The physics of dust coagulation and the structure of dust aggregates in space. *Astrophys. J.* **480**, 647–673.

Elena, M., Urso, D., Lawrence, C. J. & Michael, J. A. 1999 Pendular, funicular, and capillary bridges: results for two dimensions. *J. Colloid Interface Sci.* **220**, 42–56.

Ennis, B. J., Tardos, J. L. G. & Pfeffer, R. 1991 A microlevel-based characterization of granulation phenomena. *Powder Technd.* **65**, 257–272.

Ertas, D. & Halsey, T. C. 2002 Granular gravitational collapse and chute flow. *Europhys. Lett.* **60**, 931–935.

Félix, G. & Thomas, N. 2004 Relation between dry granular flow regimes and morphology of deposits: formation of levées in pyroclastic deposits. *Earth Planet. Sci. Lett.* **221**, 197–213.

Forsyth, A. J., Hutton, S. & Rhodes, M. J. 2002 Effect of cohesive interparticle force on the flow characteristics of granular materials. *Powder Technol.* **126**, 150–154.

Fraysse, N., Thomé, H. & Petit, L. 1999 Humidity effect on the stability of sandpile. *Eur. Phys. J.* B **11**, 615.

Fuller, F. & Tabor, D. 1975 The effect of surface roughness on the adhesion of elastic solids. *Proc. R. Soc. Lond.* **345**, 327–342.

Gady, B., Schleef, D. & Reifenberger, R. 1996 Identification of electrostatic and van der Waals forces between a micrometer-size sphere and flat surface. *Phys. Rev.* B **53**, 8065.

GDR MiDi 2004 On dense granular flows. *Euro. Phys. J.* E **14**, 341–365.

Gilabert, F. A., Roux, J.-N. & Castellanos, A. 2007 Computer simulation of model cohesive powders: influence of assembling procedure and contact laws on low consolidation states. *Phys. Rev.* E **75**, 011303.

Hatzes, A. P., Briges, F., Lin, D. N. C. & Sachtjen, S. 1991 Coagulation of particules in Saturn's rings: Measurements of the cohesive force of water frost. *Icarus* **89**, 113–121.

Hertz, H. 1881 On the contact of elastic bodies. *J. Reine Angew. Math.* **92**, 156–171.

Hornbaker, D. R., Albert, I., Barabasi, A.-L. & Schiffer, P. 1997 What keeps sandcastles up. *Nature* **387**, 765–766.

Hutter, K. R. & Rajagopal, K. R. 1994 On flow of granular materials. *Cont. Mech. Thermodyn.* **6**, 81–139.

Iordanoff, I., Berthier, Y., Descartes, S. & Heshmat, H. 2001 A review for recent approaches for modelling third bodies. *J. Tribol.* **124**, 725–735.

Iordanoff, I., Sève, B. & Berthier, Y. 2002 Solid third body analysis using a discrete approach: influence of adhesion and particle size on the macroscopic behavior of the contact. *J. Tribol.* **124**, 530–538.

Iordanoff, I., Fillot, N. & Berthier, Y. 2005 Numerical study of a thin layer of cohesive particles under plane shearing. *Powder Technol.* **159**, 46–54.

Israelachvili, J. 1992 *Intermolecular and Surface Forces.* San Diego.

Johnson, K. L. 1985 *Contact Mechanics.* Cambridge University Press.

Johnson, K. L., Kendall, K. & Roberts, A. D. 1971 Surface energy and contact of elastic solids. *Proc. R. Acad. Lond.* A **324**, 301–324.

Jones, R., Pollock, H. M., Geldart, D. & Verlinden-Luts, A. 2004 Frictional forces between cohesive powder particules studied by AFM. *Ultramicroscopy* **100**, 59–78.

Josserand, C., Lagree, P.-Y. & Lhuillier, D. 2004 Stationary shear flows of dense granular materials: a tentative continuum modelling. *Euro. Phys. J.* E **14**, 127–135.

Kadau, D., Bartels, G., Brendel, L. & Wolf, D. E. 2002 Contact dynamics simulations of compacting cohesive granular systems. *Comput. Phys. Commun.* **147**, 190–193.

Kendall, K. 1993 Significance of interparticle forces to powder behaviour. In *Powders and Grains* (ed. C. Thornton), pp. 25–31. A. A. Balkema.

Kendall, K. 1994 Adhesion: molecules and mechanics. *Science* **263**, 1720–1725.

Kim, H. & Arastoopour, H. 2002 Extension of kinetic theory to cohesive particule flow. *Powder Technol.* **122**, 83–94.

Klausner, J. F. 2000 Experimental investigation of cohesive powder rheology. *Powder Technol.* **112**, 94–101.

Lätzel, M., Luding, S. & Hermann, H. J. 2000 Macroscopic material properties from quasi-static, microscopic simulations of a two-dimensional shear-cell. *Gran. Matt.* **2**, 123–135.

Lees, A. W. & Edwards, S. F. 1972 The computer study of transport processes under extreme conditions. *J. Phys.* C **5**, 1921–1929.

Luding, S., Tykhoniuk, R. & Thomas, J. 2003 Anisotropic material behavior in dense, cohesive powders. *Chem. Engng Sci.* **12**, 1229–1232.

Mason, T. G., Levine, A. J., Hertas, D. & Hasley, T. C. 1999 The critical angle of wet granular sand piles. *Phys. Rev.* E **60**, R5044.

Mattutis, H. G. & Schinner, A. 2001 Particule simulation of cohesive granular materials. *Intl J. Mod. Phys.* C **12**, 1011–1021.

Maugis, D. 1992 Adhesion of spheres: the JKR-DMT transition using a Dugdale model. *J. Colloid Interface Sci.* **150**, 243–269.

Mei, R., Shang, H., Walton, O. & Klausner, J. 2000 Concentration non-uniformity in simple shear flow of cohesive powders. *Powder Technol.* **112**, 102–110.

Miclea, C., Tanasoiu, C., Miclea, C. F., Sima, F. N. & Cioangher, M. 2005 Influence of forming pressure of compacted powders on densification of sintered body. In *Powders and Grains 2005* (ed. R. Garcia-Rojo, H. J. Herrmann & S. McNamara), pp. 655–658. A. A. Balkema.

Mills, P., Rognon, P. G. & Chevoir, F. 2005 Transient rigid clusters in dense granular flows. In *Powders and Grains 2005* (ed. R. Garcia-Rojo, H. J. Herrmann & S. McNamara), pp. 365–369. A. A. Balkema.

Nase, S. T., Vargas, W. L., Abatan, A. & McCarthy, J. J. 2001 Discrete characterization tools for cohesive granular material. *Powder Technol.* **116**, 214–223.

Nedderman, R. M. 1992 *Statics and Kinematics of Granular Materials*. Cambridge University Press.

O'Hern, C., Langer, S. A., Liu, A. J. & Nagel, S. R. 2001 Force distributions near the jamming and glass transitions. *Phys. Rev. Lett.* **86**, 111.

Ovarlez, G. & Clément, E. 2003 Slow dynamics and aging of a confined granular flow. *Phys. Rev.* E **68**, 031302.

Pitois, O. 1999 Assemblies of lubrificated grains: development of an experimental model system and study of the contact law. PhD thesis, Ecole Nationale des Ponts et Chaussées, in french.

Pouliquen, O. 1999 Scaling laws in granular flows down a rough inclined plane. *Phys. Fluids* **11**, 542–548.

Pouliquen, O. 2004 Velocity correlation in dense granular flows. *Phys. Rev. Lett.* **93**, 248001.

Pouliquen, O. & Chevoir, F. 2002 Dense flows of dry granular materials. *C. R. Phys.* **3**, 163–175.

Pouliquen, O. & Forterre, Y. 2002 Friction law for dense granular flow: application to the motion of a mass down a rough inclined plane. *J. Fluid Mech.* **453**, 133–151.

Prochnow, M. 2002 Dense flows of dry grains. PhD thesis, Ecole Nationale des Ponts et Chaussées, http://pastel.paristech.org/archive/00000321.

Quintanilla, M. A. S, Castellanos, A. & Valverde, J. M. 2003 Interparticle contact forces in fine cohesive powders. *Proc. Appl. Math. Mech.* **3**, 206.

Radjaï, F., Jean, M., Moreau, J. J. & Roux, S. 1996 Force distributions in dense two-dimensional granular systems. *Phys. Rev. Lett.* **77**, 274–277.

Radjaï, F., Preechawuttipong, I. & Peyroux, R. 2001 Cohesive granular texture. In *Continuous and Discontinuous Modelling of Cohesive Frictional Materials* (ed. P. A. Vermeer, S. Diebels, W. Ehlers, H. J. Herrmann, S. Luding & E. Ramm), pp. 148–159. Springer.

Rajchenbach, J. 2000 Granular flows. *Adv. Phys.* **49**, 229–256.

Richard, P., Philippe, P., Barbe, F., Bourles, S., Thibault, W. & Bideau, D. 2003 Analysis by X-ray microtomography of a granular packing undergoing compaction. *Phys. Rev.* E **68**, 020301.

Richefeu, V., El Youssoufi, M. S., Peyroux, R. & Bohatier, C. 2005 Frictional contact and cohesion laws for Casagrande's shear test on granular materials by 3D DEM – comparison with experiments. In *Powders and Grains 2005* (ed. R. Garcia-Rojo, H. J. Herrmann & S. McNamara), pp. 509–513. A. A. Balkema.

Richefeu, V., El Youssoufi, M. S. & Radjaï, F. 2006 Shear strength properties of wet granular materials. *Phys. Rev.* E **73**, 051304.

Rietema, K. 1991 *The Dynamics of Fine Powders.* Elsevier.

Rivier, N. 2005 Granular matter with even circuits: ball-bearing and dry quicksand. In *Powders and Grains 2005* (ed. R. Garcia-Rojo, H. J. Herrmann & S. McNamara), pp. 29–32. A. A. Balkema.

Rognon, P. G., Roux, J.-N., Wolf, D., Naaim, M. & Chevoir, F. 2006 Rheophysics of cohesive granular materials. *Europhys. Lett.* **74**, 644–650.

Rognon, P. G., Chevoir, F., Bellot, H., Ousset, F., Naaim, M. & Coussot, P. 2007 Rheology of dense snow flows. *J. Rheol.* (Submitted).

Roux, J. N. & Chevoir, F. 2005 Discrete numerical simulations and mechanical behaviour of granular materials. *Bull. Lab. Ponts Chaussées* **254**, 109–138.

Roux, J. N. & Combe, G. 2002 Quasistatic rheology and the origins of strain. *C. R. Phys.* **3**, 131–140.

Rumpf, H. 1958 Grundlagen und Methoden des Granulierens. 1. Teil: Begriffe Anwendungen und Eigenschaften der Granulate. *Chem. Ing. Tech.* **30**.

Samandani, A. & Kudrolli, A. 2001 Angle of repose and segregation in cohesive granular matter. *Phys. Rev.* E **64**, 1–9.

Silbert, S. L., Ertas, D., Grest, G. S., Halsey, T. C., Levine, D. & Plimpton, S. J. 2001 Granular flow down an inclined plane. *Phys. Rev.* E **64**, 385–403.

Taboada, A., Estrada, N. & Radjaï, F. 2006 Additive decomposition of shear strength in cohesive granular media from grain-scale interactions. *Phys. Rev. Lett.* **97**, 098302.

Tabor, D. 1981 Friction – the present understanding. *J. Lubrication* **103**, 169–179.

Talu, I., Tardos, G. I. & Ruud van Ommen, J. 2001 Use of stress fluctuations to monitor wet granulation of powders. *Powder Technol.* **117**, 149–162.

Tegzes, P., Albert, R., Paskvan, M., Barabasi, A.-L., Viczek, T. & Schiffer, P. 1999 Liquid-induced transitions in granular media. *Phys. Rev.* E **60**, 5823–5826.

Tegzes, P., Viczek, T. & Schiffer, P. 2002 Avalanche dynamics in wet granular materials. *Phys. Rev. Lett.* **89**, 1–4.

Tegzes, P., Viczek, T. & Schiffer, P. 2003 Development of correlations in the dynamics of granular avalanches. *Phys. Rev.* E **67**, 051303.

Thornton, C. 1997 Coefficient of restitution for collinear collisions of elastic perfectly plastic spheres. *Trans. ASME* E: *J. Appl. Mech.* **64**, 383–386.

Tomas, J. 2004 Fundamentals of cohesive powder consolidation and flow. *Gran. Matt.* **6**, 75–86.

Valverde, J. M., Castellanos, A. & Ramos, A. 2000 Avalanches in fine, cohesive powders. *Phys. Rev.* E **62**, 6851–6861.

Weber, M. W., Hoffman, D. K. & Hrenya, C. M. 2004 Discrete-particle simulations of cohesive granular flow using a square-well potential. *Gran. Matt.* **6**, 239–254.

Wolf, D. E., Unger, T., Kadau, D. & Brendel, L. 2005 Compaction of cohesive powders. In *Powders and Grains 2005* (ed. R. Garcia-Rojo, H. J. Herrmann & S. McNamara), pp. 525–535. A. A. Balkema.